

# Self-Aligning Finger Exoskeleton for the Mobilization of the Metacarpophalangeal Joint

Emanuele Peperoni<sup>1</sup>, Stefano Laszlo Capitani, Tommaso Fiumalbi<sup>2</sup>, Eugenio Capotorti, Andrea Baldoni<sup>3</sup>, Filippo Dell'Agnello<sup>4</sup>, Ilaria Creatini, Elisa Taglione<sup>5</sup>, Nicola Vitiello<sup>6</sup>, *Member, IEEE*, Emilio Trigili<sup>7</sup>, *Member, IEEE*, and Simona Crea<sup>8</sup>, *Member, IEEE*

**Abstract**—In the context of hand and finger rehabilitation, kinematic compatibility is key for the acceptability and clinical exploitation of robotic devices. Different kinematic chain solutions have been proposed in the state of the art, with different trade-offs between characteristics of kinematic compatibility, adaptability to different anthropometries, and the ability to compute relevant clinical information. This study presents the design of a novel kinematic chain for the mobilization of the metacarpophalangeal (MCP) joint of the long fingers and a mathematical model for the real-time computation of the joint angle and transferred torque. The proposed mechanism can self-align with the human joint without hindering force transfer or inducing parasitic torque. The chain has been designed for integration into an exoskeletal device aimed at rehabilitating traumatic-hand patients. The exoskeleton actuation unit has a series-elastic architecture for compliant human-robot interaction and has been assembled and preliminarily tested in experiments with eight human subjects. Performance has been investigated in terms of (i) accuracy of the MCP joint angle estimation through comparison with a video-based motion tracking system, (ii) residual MCP torque when the exoskeleton is controlled to provide null output impedance and (iii) torque-tracking performance.

Manuscript received 5 August 2022; revised 29 December 2022; accepted 4 January 2023. Date of publication 11 January 2023; date of current version 3 February 2023. This work was supported in part by the Italian National Institute for Insurance Against Accidents at Work (Inail), in part by the HABILIS Project, and in part by the HABILIS++ Project under Grant PR19-RR\_P4. (Emanuele Peperoni and Stefano Laszlo Capitani contributed equally to this work. Emilio Trigili and Simona Crea share the senior authorship.) (Corresponding authors: Emanuele Peperoni; Simona Crea.)

This work involved human subjects or animals in its research. Approval of all ethical and experimental procedures and protocols was granted by the Local Ethics Committee, Comitato Etico Area Vasta Nord-Ovest Toscana under Approval No. 18756.

Emanuele Peperoni, Stefano Laszlo Capitani, Tommaso Fiumalbi, Andrea Baldoni, Filippo Dell'Agnello, and Emilio Trigili are with The BioRobotics Institute, Scuola Superiore Sant'Anna, 56025 Pisa, Italy, and also with the Department of Excellence in Robotics and AI, Scuola Superiore Sant'Anna, 56127 Pisa, Italy (e-mail: emanuele.peperoni@santannapisa.it).

Eugenio Capotorti was with The BioRobotics Institute, Scuola Superiore Sant'Anna, 56025 Pisa, Italy. He is now with Johnson & Johnson Medical Spa, 00071 Rome, Italy (e-mail: eugenio.capotorti@gmail.com).

Ilaria Creatini and Elisa Taglione are with the Motor Rehabilitation Center, National Institute for Insurance Against Accidents at Work (INAIL), 56048 Pisa, Italy.

Nicola Vitiello and Simona Crea are with The BioRobotics Institute, Scuola Superiore Sant'Anna, 56025 Pisa, Italy, also with the Department of Excellence in Robotics and AI, Scuola Superiore Sant'Anna, 56127 Pisa, Italy, and also with the IRCCS Fondazione Don Gnocchi, 50143 Florence, Italy (e-mail: simona.crea@santannapisa.it).

Digital Object Identifier 10.1109/TNSRE.2023.3236070

Results showed a root-mean-square error (RMSE) below 5 degrees in the estimated MCP angle. The estimated residual MCP torque resulted below 7 mNm. Torque tracking performance shows an RMSE lower than 8 mNm in following sinusoidal reference profiles. The results encourage further investigations of the device in a clinical scenario.

**Index Terms**—Rehabilitation robotics, kinematic compatibility, human-robot interfaces, hand, exoskeleton.

## I. INTRODUCTION

UPPER-LIMB impairments resulting from hand injuries, rheumatic diseases such as rheumatoid arthritis and osteoarthritis, and long-term consequences of hand burns and infection highly affect the capability of patients to perform common activities of daily living. Typical consequences of such impairments include reduced finger range of motion (ROM) and strength, as well as increased joint stiffness [1]. Almost all finger injuries can cause joint stiffness, even when the joint is not directly damaged. Both bone and soft tissue involvement can induce mechanical blocks to motion, resulting in finger stiffness [2]. The stiffening of the metacarpophalangeal (MCP) joint in an extended position strongly limits the performance of patients in common grasping and pinching tasks, thus it is commonly treated as a first-line intervention using surgery and rehabilitation techniques [3].

In the context of robot-aided rehabilitation, the design of wearable robots for the fingers poses major challenges from a bioengineering viewpoint. Indeed, the natural structure of the finger allows for a high ROM and fine torque control over multiple degrees of freedom (DOFs), exploiting under-actuation via both intrinsic and extrinsic muscles. For a robotic device for post-traumatic rehabilitation to mimic such features, a tradeoff between characteristics of kinematic compatibility, joint range of motion, adaptability to different anthropometries, ability to compute relevant clinical information, and encumbrance is needed [4], [5].

In literature, two main robotic architectures for finger/hand rehabilitation have been introduced, namely soft *exogloves* and rigid exoskeletons. Soft *exogloves* rely on stretchable fabrics anchored at key points around human joints to transfer shear forces to the user (hence, generating joint moments), via pneumatic or cable-driven transmission systems acting in parallel with the biological muscle-tendon structures [6], [7]. The kinematic alignment of the *exoglove* to the biological structure is achieved through the routing of the artificial

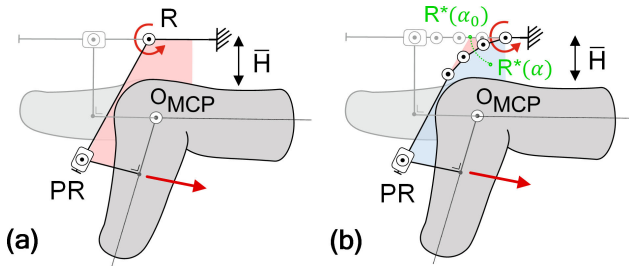


Fig. 1. (a) RPR chain design, and its expected dorsal encumbrance on a flexed finger (red area). (b) Equivalent RPR chain with the series of hinges proposed in this work, with the indication of the equivalent hinge movement ( $R^*(\alpha)$ ) during finger flexion and the expected dorsal encumbrance (blue area).

transmission means and the positioning of the anchoring points on the human finger. Soft structures have an intrinsically low weight and encumbrance, but they may not be appropriate when the application of shear forces to the underlying musculotendon structures could cause damage and are limited in the amount of torque that can be transferred to articulations since textiles or rubber-like materials exhibit low stiffness [8], [9]. In addition, a precise measurement of biomechanical quantities (e.g., angles, velocities, torques) is challenging, because soft structure prevents sensors from being solidly anchored to a fixed reference frame. Conversely, rigid exoskeletons are potentially able to deliver a larger amount of torque on each finger joint, allowing at the same time for a more reliable measurement of biomechanical parameters [10], [11]. The alignment between the human and robot joint axes is necessary to avoid reactive loads on the human musculoskeletal structure, therefore self-alignment mechanisms are usually considered in the kinematic design. Collocating the robot axes directly in line with the ones of the human joints would require the kinematic chain to fit the fingers laterally, limiting the possibility to actuate more fingers simultaneously. Hence, *remote center of motion* (RCM) architectures running along the fingers' dorsal side may be preferred. Different RCM kinematic chains can be designed by combinations and permutations of rotational (R) and prismatic (P) joints. For a rigid-link RCM architecture with one DOF (i.e., MCP flexion/extension), at least three joints are needed to realize a self-alignment mechanism [12]. PRP chains can be easily designed to be mechanically coupled in serial joints [13], but the prismatic joints require long sliders to have a sufficient stroke to cover a functional ROM [14]. RRR chains often result in a large dorsal encumbrance, necessary to avoid interference with the finger when a large ROM is needed, and shear reaction forces on the soft tissues are not negligible [15], [16]. Finally, an RPR architecture allows for a further reduction of dorsal encumbrance [14] but it requires the first rotational joint to be placed distally on the finger to reduce the risk of collision between the robot and human limb (Fig. 1a).

In this paper, a novel kinematic chain for the MCP joint of the index finger is presented. The chain is based on an RPR design, in which the first rotational DOF is spread into a series of hinges connected by gears, equivalent to a virtual hinge  $R^*(\alpha)$ , to comply with finger flexion/extension movements

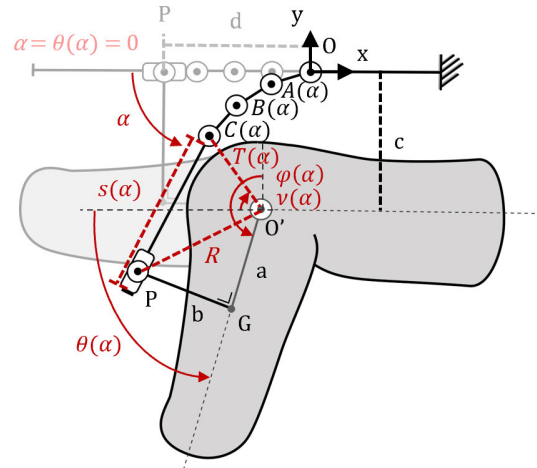


Fig. 2. In light color, the closed kinematic chain between the finger and exoskeleton in the reference condition (extended finger). In heavy color the configuration during finger flexion. The radius  $R$ , the stroke  $s$  of the slider-hinge joint and the exoskeleton angle  $\alpha$  are highlighted in red, together with the  $\alpha$ -dependent variables used to derive the MCP angle  $\theta$ .

while maintaining a low dorsal encumbrance. Compared to classical RPR implementations, the equivalent hinge allows for a high ROM within a lower volume over the finger during flexion/extension (see the comparison between blue and red areas in Fig. 1b). The final P-R joints ensure that forces are transferred perpendicularly to the finger phalanx, minimizing reactive loads to the MCP articulation and shear forces to the soft tissues. The kinematic chain was implemented on a finger exoskeleton with a miniaturized series-elastic actuator (SEA) for the mobilization of the index MCP joint in post-traumatic hands and compliant human-robot interaction. A kineto-static model of the system was developed to estimate the MCP joint angle and torques based on the information provided by the exoskeleton's embedded sensors. Thus, the exoskeleton can estimate the MCP joint angle and torque, allowing for personalized rehabilitation treatments and biomechanical assessments.

The paper is structured as follows. Section II presents the model of the robot kinematic chain closed to the human MCP joint, to estimate the MCP joint angle. Section III describes the implementation of the kinematic chain on a finger exoskeleton for the MCP joint with a miniaturized SEA. In section IV, the mechatronic characterization of the finger exoskeleton is presented while section V presents the kinematic and kineto-static verification of the exoskeleton with participants without any known hand disability or pain. Finally, the results are discussed in section VI.

## II. KINEMATIC CHAIN MODELLING

A closed kinematic model with the robot kinematic chain and the human finger has been developed (Fig. 2). The closed-loop chain results in one free DOF, i.e., the MCP flexion angle (hereafter  $\theta$ ). The developed model is here presented in the case of a fixed number of hinges, namely four, but the analytical formulation holds also in the case of a different number of hinges. The global reference frame is in correspondence with

the first hinge of the robot kinematic chain (centered in  $O$ ), and the MCP frame is centered in  $O'$ .

For the modelling purpose, the “reference condition” (Fig. 2, light color) is defined as the condition in which the kinematic chain is parallel to the horizontal axis (i.e., the angle between the slider-hinge joint and the horizontal axis,  $\alpha$ , is null). In this condition, considering  $G$  as the orthogonal projection of  $P$  onto the proximal phalanx axis ( $PG \perp GO'$ ), the closed kinematic chain can be described by a trapezoid, with links  $OP$ ,  $PG$ ,  $GO'$  and  $O'O$  initialized to:

$$|P - O| = d; \quad (1)$$

$$|G - P| = b; \quad (2)$$

$$|O' - G| = a; \quad (3)$$

$$|O' - O| = \sqrt{c^2 + (d - a)^2} \quad (4)$$

where  $c$  is the vertical distance between points  $O$  and  $O'$ . Values  $a$ ,  $b$ ,  $c$ ,  $d$  are in this section considered known. When the phalange rotates around  $O$  of  $\theta$ , point  $P$  moves along the slider so that the condition  $PG \perp GO'$  is maintained. Considering that the angle  $\alpha$  is known,  $\theta$  can be extracted as a function of  $\alpha$ , following the steps described below:

1. considering the rotation of the hinges that compose the kinematic chain (in the case shown in Fig. 2 four hinges rotate around points  $O$ ,  $A$ ,  $B$ ,  $C$ ), the position of point  $C(\alpha)$  can be expressed as:

$$\begin{aligned} C(\alpha) &= \begin{pmatrix} C_x(\alpha) \\ C_y(\alpha) \end{pmatrix} = (|A - O| + |B - A| + |C - B|) \\ &= 2r \begin{pmatrix} \cos\left(\frac{\alpha}{4} + \pi\right) + \cos\left(2\frac{\alpha}{4} + \pi\right) + \cos\left(3\frac{\alpha}{4} + \pi\right) \\ \sin\left(\frac{\alpha}{4} + \pi\right) + \sin\left(2\frac{\alpha}{4} + \pi\right) + \sin\left(3\frac{\alpha}{4} + \pi\right) \end{pmatrix} \end{aligned} \quad (5)$$

where  $r$  is the pitch radius of the hinges, hence all hinges rotate by the same angle  $\frac{\alpha}{4}$ ;

2. being  $O$  and  $C$  known, the distance between the point  $C$  and  $O$ , namely  $T(\alpha)$ , can be extracted;
3.  $v(\alpha)$  is defined as the angle between the segment  $T(\alpha)$  and the horizontal axis:

$$v(\alpha) = \arcsin\left(\frac{|C_x(\alpha) - O'_x|}{T(\alpha)}\right); \quad (6)$$

4. the distance between points  $P$ , which describes a circular trajectory with a constant radius  $R$  around  $O'$ , and  $C$ , namely  $s(\alpha)$ , can be computed by applying the *law of cosines* to the  $PCO$  triangle as:

$$\begin{aligned} s(\alpha)^2 - 2T(\alpha) \cdot s(\alpha) \cdot \cos(\pi - \alpha - v(\alpha)) \\ + T(\alpha)^2 - R^2 = 0; \end{aligned} \quad (7)$$

5. once the coordinates of  $P$  are known, angle  $\varphi(\alpha)$  is:

$$\begin{aligned} \varphi(\alpha) &= \tan^{-1}\left(\frac{-|P_x(\alpha) - O'_x|}{|P_y(\alpha) - O'_y|}\right) \\ &= \tan^{-1}\left(\frac{-|C_x(\alpha) - O_x| - s(\alpha)\cos(\alpha)}{|C_y(\alpha) - O_y| - s(\alpha)\sin(\alpha)}\right); \end{aligned} \quad (8)$$

6. finally, it is possible to compute the angle  $\theta$  as:

$$\theta(\alpha) = \varphi(\alpha) - \varphi(\alpha = 0) \quad (9)$$

### III. MECHATRONIC PROTOTYPE

#### A. Functional Requirements

To test the performance of the proposed self-aligning mechanism and determine its applicability in a wearable robot, a finger exoskeleton based on the proposed kinematic chain has been developed, named I-PhlEx. The robot was designed for application in occupational therapy, to mimic the mobilization exercises typical of occupational treatments. Specifically, treatments usually start with physical therapists performing passive mobilization of the fingers to relieve the stiffness on tendinous structures and to regain progressively the range of motion; sessions then include active mobilization exercises within the pain-free ROM. Rehabilitation is recommended to start immediately after the surgery or the traumatic event to avoid complications. Since joints and tissues are particularly fragile in the early phase, the success of the rehabilitation is strongly dependent on the ability and expertise of therapists to dose forces/torques during the therapy, without overcoming the patient's pain-free ROM. Robotic platforms designed to help clinicians in this phase should allow for (i) a safe torque transfer to the fingers during the rehabilitation, limiting parasitic forces on the human joint and shear forces at the human-robot interface, and (ii) accurate measurement of the biomechanical parameters that are relevant for a safe treatment (e.g. real-time angle and torque) and offline evaluation of the therapy progress (e.g. active and passive ROM).

Given these considerations, a list of technical requirements for the design of the I-PhlEx exoskeleton has been derived. The device was designed for:

- passively and actively assisting the MCP joint movement in the sagittal plane (flexion/extension - F/E movement);
- covering a range of motion of the MCP joint between 0 and at least 70 deg;
- embedding a self-alignment mechanism able to cope with MCP F/E movement and ensure kinematic compatibility [17];
- measuring and controlling the torque exerted on the joint over a suitable range, stated up to 1 Nm [18];
- being used with at least the 50<sup>th</sup> percentile of hand anthropometries [19].

The resulting prototype is composed of the proposed kinematic chain, a series-elastic-based actuation unit, an electronic box, and physical human-robot interfaces (pHRIs) to connect the robot to the user's fingers.

#### B. Kinematic Chain

As shown in Fig. 3a, the first rotational element of the RPR chain is conceived with spur gear meshes. The arrangement is composed of three internal gear meshes and four external ones that are coupled alternately, resulting in four hinges. Each gear has a module of 0.5 mm and a pitch diameter of 7.5 mm, is manufactured in Maraging steel (Böhler w720), and is capable to bear up to 2 Nm. The number of gears can be adjusted

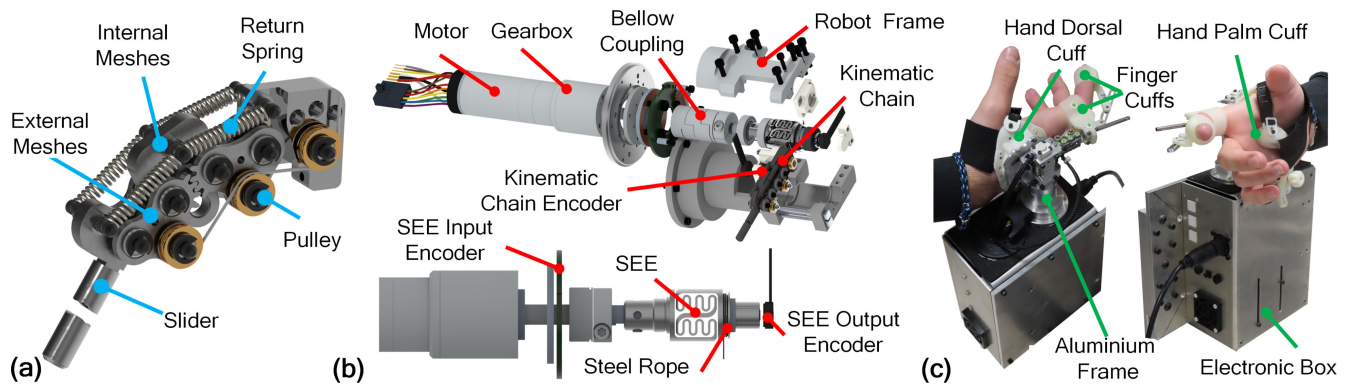


Fig. 3. Overview of the I-Phlex exoskeleton. (a) Assembly of the kinematic chain components. (b) Exploded assembly of the actuation unit. (c) Layout of the system with the pHRIs (finger and hand cuffs). Acronym: SEE, Series Elastic Element.

to fit the phalanges of different fingers according to their length; the minimum set corresponds to two internal gears and an external one (i.e., two hinges). Additional details can be found in the related patent [20]. In this study, the kinematic chain was prototyped considering the average dimensions of the index finger, i.e. MCP diameter of 25 mm, proximal interphalangeal (PIP) joint diameter of 20 mm, and proximal phalanx of 60 mm [19]. To fit such dimensions, four hinges were considered adequate. The resulting chain is 32 mm long with a dorsal encumbrance of 12 mm. The distal mesh is connected to a linear guide of 34 mm in length, which is the rail of the slider-hinge joint of the chain.

A parametric model of the kinematic chain was used to estimate the volume reduction with respect to the traditional implementation of an equivalent RPR chain. The inputs to the model were the ROM of the MCP joint (90 deg), the anthropometric dimensions of a 50th percentile finger [19], the height of the chain over the dorsum ( $\bar{H}$ ) equal in both chains (12 mm), and the position of the finger cuff to have orthogonality between the slider hinge joint and the phalanx (see Fig. 1 and Fig. 2). The occupied volume above the finger is the space enclosed between the finger dorsum and the robot's chain. Hence, for the same width of the chain, the volume reduction over a classical RPR chain is equal to 13% (relative difference between the blue area and the red area in Fig. 1b).

### C. Electronic Box and Actuation Unit

The electronic box hosts: a control electronics unit (custom board with a SOM SbrIO-9651, National Instruments®, Texas, US - endowed with a Linux®RT processor and a Zynq-7020 FPGA); an ELMO Gold Twitter driver (ELMO Motion Control®, Petach-Tikva, Israel); a DC motor (Brushless Maxon® ECX SP22M 24V endowed with Incremental Encoder ENX 22 EASY INT 1024 pulses, Maxon Motor ag ©, Sachseln, Switzerland) connected to a planetary gearbox (Maxon®GPX 26 LZ 111:1 reduction ratio, Maxon Motor ag ©, Sachseln, Switzerland) and the connection to an external power supply. From the gearbox, the shaft of the actuator is connected to a miniaturized series-elastic element (SEE) using a bellow coupling (Fig. 3b). Two absolute magnetic encoders are used to measure the deformation of the elastic element: an

RLS® AksIM-2 18 bit (RLS Merilna Tehnika®, Slovenia) at the output of the gearbox, thus at the SEA input, and an RLS® RM08 12 bit (RLS Merilna Tehnika ©, Slovenia) embedded in the robot frame on the spring output (Fig. 3b). The miniaturized torsional spring ([11], [21]) has a serpentine shape occupying a cylindrical volume of 15.5 mm in diameter and 15.5 mm in length. The spring stiffness of 2.89 Nm/rad was selected to have a torque resolution of at least 10 mNm to control torques up to 1 Nm (namely 4.4 mNm torque resolution with the 12-bit encoder) [16], and structural strength to bear torsional loads up to at least 1 Nm (namely 1.5 Nm via simulation with Ansys software – Ansys Inc., PA, US). To transmit torque to the joint, two antagonistic transmission systems act in parallel. To transmit flexion torque, a steel rope on the output of the actuation unit is routed on three driven pulleys with the same primitive radius and anchored at the opposite side of the chain, whereas finger extension is obtained using return springs fixed on the upper part of the chain (Fig. 3a). A third RLS® RM08 12-bit encoder (RLS Merilna Tehnika ©, Slovenia) is placed on the first mesh of the kinematic chain and is used to measure the exoskeleton joint angle,  $\alpha_0$ . In the four-hinges configuration, the angle  $\alpha_0$  measured by the encoder placed on the first mesh results in  $\alpha = 4 \cdot \alpha_0$  at the end of the series of meshes. The system results in a ROM of the MCP joint between 0 and 90 deg, which is suitable for the application [22].

### D. Hand and Finger Cuffs

The pHRIs are composed of two parts, depicted in Fig. 3c: the hand cuff, to connect the hand to the robot frame through dorsal and palmar elements, and the finger cuffs, positioned on the first phalanx and fingertip. The dorsal hand cuff is connected to the actuation through a rigid aluminium frame anchored to the robot frame. To fit different hand sizes, the position of this frame can be adjusted in both anteroposterior and mediolateral directions (with respect to the hand dorsum) using rails embedded in the aluminium structure. The palmar hand cuff helps to hold the hand stably. The pressure against the palm can be adjusted using a knob during the don/doff procedure. Both dorsal and palmar hand cuffs are made in 3D-printed ABS material, modelled to fit the anatomical curvature of the hand dorsum and palm, and the parts in contact

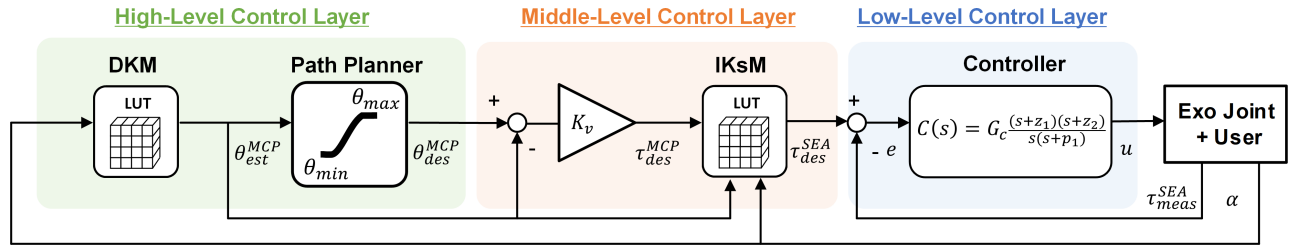


Fig. 4. Control architecture of the I-PhlEx exoskeleton. The high-level control layer calculates the MCP angle through a look-up table (LUT) implementing the direct kinematic model (DKM) and sets the reference for the angular movement through a path planner block. The middle-level controller is dedicated to the implementation of an impedance controller and a LUT for the inverse kineto-static model (IKsM) to compute the desired SEA torque. Finally, the low-level control layer sets commands to the actuator to follow the torque reference through a lead-lag controller in a feedback loop configuration.

with the user's skin are covered in silicon material. This configuration makes the contact pressure uniformly distributed over a wide area and the interface comfortable for the user. The finger cuffs are two: a proximal cuff connected to the proximal finger phalanx, and a distal one anchored to the fingertip. They are made of ABS and the part in contact with the skin is covered in silicon. The slider-hinge joint is embedded inside an ABS structure of the finger proximal cuff. The distal cuff is connected to the proximal cuff using two rigid bars connected through an eyelet, which makes the relative angle between the bars adjustable in the preferred configuration. Both hand and finger cuffs have been designed for different sizes to accommodate different hand and finger anthropometries.

### E. Kineto-Static Model

Based on the kinematic relationship described in Section II, a kineto-static model of the finger-exoskeleton kinematic chain has been defined, to evaluate the force transferred by the exoskeleton to the MCP joint through the antagonistic transmission system described in Section III-C. The model is grounded on the *virtual-works principle* (VWP), considering the following forces acting on the system: (i) the SEA torque  $\tau_{SEA}$ , (ii) the return springs force  $K_m \cdot x(\alpha)$ , and (iii) the torque at the MCP  $\tau_{MCP}$ . It is possible to define  $\psi$  as the angle measured at the output of the SEE but referred to the first mesh of the kinematic chain (point  $O$  in Fig. 2).  $\psi$  can be related to the kinematic chain angle  $\alpha$  by the following relation:

$$\psi = \alpha / \lambda \quad (10)$$

where  $\lambda$  is the reduction ratio between the SEA output angle and the first hinge angle. A value of 2.07 for  $\lambda$  was obtained from a multibody simulation of the kinematic chain in a MATLAB-Simulink environment (MATLAB 2021a, The MathWorks, Inc., MA, US). By expressing the differential quantities as a function of the angle  $\alpha$ , the VWP can be formulated as:

$$\tau_{SEA} d\psi(\alpha) = K_m x(\alpha) dx(\alpha) + \tau_{MCP} d\theta(\alpha) \quad (11)$$

Thus, the estimation of the torque at the joint level is given by:

$$\tau_{MCP} = \frac{\tau_{SEA} \psi'(\alpha) - K_m x(\alpha) x'(\alpha)}{\theta'(\alpha)} \quad (12)$$

Since the VWP formulation does not hold under dynamic conditions, the solution shall be considered correct for a quasi-static operation of the exoskeleton, i.e., at low velocities.

### F. Control Architecture

The control architecture of the I-PhlEx platform is designed to passively mobilize the index MCP joint, mimicking the action of the occupational therapist, or, when the patient presents a residual movement capability, to assist finger flexion along the sagittal plane, implementing an *assist-as-needed* strategy. The two different paradigms have been categorized previously in the state of the art as *robot-in-charge* and *patient-in-charge*, respectively [23].

The control architecture has a hierarchical structure (Fig. 4), comprising: (i) a *high-level control layer*, which implements the direct kinematic model (DKM) for the MCP angle estimation and generates the reference trajectories for the joint; (ii) a *middle-level control layer*, which sets the desired MCP torque following an impedance control law, and implements the inverse kineto-static model (IKsM) to compute the desired SEA torque; (iii) a *low-level control layer*, which implements a torque controller by setting the reference current to the motor driver. The high and middle-level control layers run on the RT processor at 100 Hz, whereas the low-level control layer is implemented on the FPGA running at 1 kHz. A graphical user interface (GUI) is implemented in LabVIEW environment to (i) set the control parameters of the high- and middle-level control layers, (ii) visualize the joint angles and torques, and (iii) save data. The visual interface (Fig. 6) displays two bars, one red and one blue, corresponding to a reference joint position and the measured angle, and is updated at each iteration of the RT processor. The visual interface is implemented in LabVIEW and launched by the GUI.

1) *High-Level Control*: The high-level control embeds the DKM for the estimation of the MCP angle ( $\theta_{est}^{MCP}$ ) from the measured angle  $\alpha$ . The DKM is implemented in the form of a look-up table (LUT). The LUT is generated offline by taking as inputs the parameters  $a$ ,  $b$  and  $c$ , measured in the reference configuration. In addition, a path planner is implemented to output minimum-jerk sigmoidal reference trajectories for the MCP joint, according to the following equation:

$$\theta_{des}^{MCP}(t) = y_i + (y_f - y_i) \left( 10 \left( \frac{t}{D} \right)^3 - 15 \left( \frac{t}{D} \right)^4 + 6 \left( \frac{t}{D} \right)^5 \right) \quad (13)$$

where the  $\theta_{des}^{MCP}(t)$  describes the generated trajectory,  $y_f$  and  $y_i$  are respectively the target angle  $\theta_{des}^{MCP}$  at  $t = D$  and the

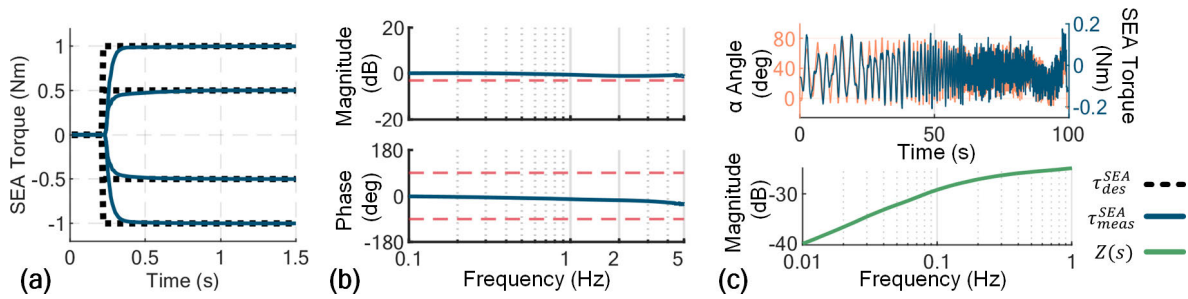


Fig. 5. Results of the bench tests. (a) Step response. Desired torques ( $\tau_{des}^{SEA}$ ) and average measured torque from the SEA ( $\tau_{meas}^{SEA}$ ) in the four step conditions. (b) Bode plots of the transfer function  $H(s)$  extracted from chirp response. Red lines indicate the  $-3$  dB threshold in magnitude plot and  $90$  deg shift in the phase plot. (c) Output impedance. Measured SEA torque ( $\tau_{meas}^{SEA}$ ) and  $\alpha$  angle during manual elicitation of the output. Below, the frequency response of the  $Z(s)$  function, namely the output mechanical impedance, normalized to the SEE stiffness, over the explored frequency range.

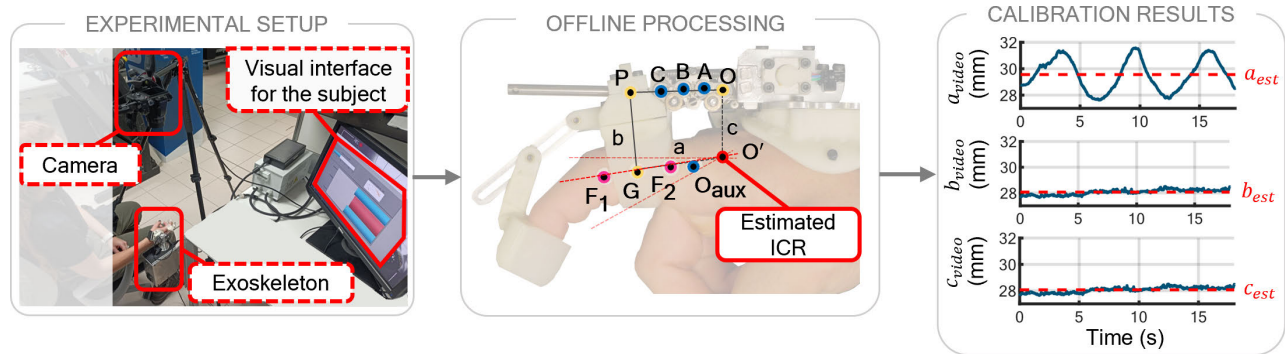


Fig. 6. Experimental set up and calibration procedure. The experimental setup is composed by the I-PhiEx exoskeleton, the camera for video recording and a screen displaying the visual interface. Once the calibration procedure is finished, data are postprocessed in Python environment. Calibration results for one subject are presented in figure. The mean values of the geometric parameters obtained in this phase (red dashed lines) has been used as reference geometric parameters for the user and as input for the LUT. The time window showed in the calibration results is obtained after the ICR position reached convergence.

initial angle  $\theta_{est}^{MCP}$  at  $t = 0$ ,  $D$  is the duration of the trajectory and  $t$  is the current time ( $t$  is set to 0 at the beginning of each trajectory). Different rehabilitation strategies can be implemented by changing the amplitude, duration, and speed of the profile. The path planner output, namely a sigmoidal function, is exploited as a reference trajectory for the users in the exercises. The signal  $\theta_{des}^{MCP}$  is displayed to the user through the visual interface, and it corresponds to the reference signal (blue bar in Fig. 6).

2) *Middle-Level Control*: The middle-level control is composed of two main blocks, the impedance control block and the IKsM.

a) *Impedance control*: This block regulates the desired MCP torque according to an impedance control law, namely proportionally to the error between the reference trajectory and the estimated MCP angle:

$$\tau_{des}^{MCP} = K_v(\theta_{des}^{MCP} - \theta_{est}^{MCP}) \quad (14)$$

The values of the virtual stiffness  $K_v$  can span from 0.005 to 0.01 Nm/deg, so that according to the virtual stiffness value, the exercise could be framed within a *patient-in-charge* or *robot-in-charge* paradigm. Notably, when the virtual stiffness  $K_v$  is set to 0, the exoskeleton works in the so-called *zero-torque* modality, namely, the desired output impedance is null.

b) *Inverse kineto-static model*: The IKsM computes the desired SEA torque ( $\tau_{des}^{SEA}$ ), knowing the desired MCP torque computed from the impedance controller. The relation is

obtained from the kineto-static model reported in Section III-E and implemented through a LUT, which takes as input  $\theta_{est}^{MCP}$ ,  $\alpha$  and the desired MCP torque  $\tau_{des}^{MCP}$ . To guarantee continuity in the torque profile, a linear interpolation occurs once the values from the LUT are sorted. Hence, the desired torque at the SEA level  $\tau_{des}^{SEA}$  is computed and exploited as a reference for the lower control layer.

3) *Low-Level Control*: The low-level regulator consists of a closed-loop torque controller that compensates for the error between the desired and measured SEA torque,  $e$ . A two-pole-two-zeros lead-lag compensator drives the system dynamics using  $e$  as a reference signal, feeding a current input  $u$  to the motor driver. The controller has been designed via a pole-placement method, based on the identification of the open-loop transfer function as in [24]. It contains an integrator to nullify steady-state errors and the gain  $G_c$  is chosen to have all closed-loop poles on the negative real axis in the complex plane.

#### IV. BENCH TESTS

To assess the actuation unit performances, three different bench tests were conducted, namely for the assessment of the torque step and chirp responses and for the evaluation of the output impedance when the device is set in the *zero-torque* modality. For two of them, namely the step and chirp response tests, the output link of the actuation unit was kept locked mechanically against the mechanical end-stop, while for the impedance test the output link was free to move.

TABLE I  
STEP RESPONSE RESULTS

Amplitude (Nm)	Rise Time (s)	Settling Time (s)
1	0.07±0.01	0.33±0.01
0.5	0.11±0.01	0.53±0.01
-0.5	0.11±0.01	0.42±0.03
-1	0.08±0.01	0.33±0.01

1) *Step Response*: Twenty increasing and decreasing torque steps of two different amplitudes ( $\pm 0.5$  Nm,  $\pm 1$  Nm) were commanded to the actuation unit. Average values and standard deviations of the rise time and settling time were calculated. The average rise time obtained for the controller was 0.09s, with an average settling time of 0.41s (Table I). All step responses had no overshoot. Average profiles are reported in Fig. 5a.

2) *Chirp Response*: Three torque chirp inputs were commanded, spanning from 0.1 Hz to 5 Hz. The transfer function between the measured and desired torque,  $H(s) = \tau_{meas}^{SEA}(s)/\tau_{des}^{SEA}(s)$ , was estimated to identify the bandwidth of the controller. Within the tested frequency range, the  $-3$ dB cut-off frequency was not reached. The *RMSE* between the desired and the measured SEA torque, computed to quantify the tracking performance at the actuation level, was  $0.065 \pm 0.005$  Nm. The phase lag was 30 deg at 5Hz. Torque bandwidth results are presented in Fig. 5b.

3) *Output Impedance*: The output mechanical impedance, defined as  $Z(s) = \tau_{meas}^{SEA}(s)/\alpha(s)$ , was investigated to evaluate the system transparency in terms of parasitic torque in the *zero-torque* modality. The output link of the actuation unit was manually moved by an experimenter following a quasi-sinusoidal movement within a frequency range between 0.01 and 1 Hz. The amplitude of the Bode plot of  $Z(s)$ , normalized to the SEE stiffness value, ranged between  $-40.05$  dB and  $-24.82$  dB on the observed frequencies. Results are reported in Fig. 5c.

## V. EXPERIMENTAL VERIFICATION

Two experimental sessions were conducted with participants without any known hand disability or pain. The first session aimed at verifying the accuracy of the kinematic model in estimating the MCP joint angle. The goal of the second session was to assess the human-in-the-loop torque-tracking performance and the *transparency* of the system in terms of residual MCP torques and output impedance in *zero-torque* modality. Eight right-handed subjects (8 males, aged  $27 \pm 4$  years) took part in the first session. Two of them were not available to participate also in the second session. The experimental protocol was approved by the local Ethics Committee, namely Comitato Etico Area Vasta Nord-Ovest Toscana (Protocol ID: HABILIS 2020; approval number: 18756) and participants signed a written informed consent before participation.

### A. Experimental Setup

The experimental setup (Fig. 6) was composed of the exoskeletal platform, a digital camera (Nikon Coolpix b500,

20frame/s, 105 mm focal zoom) to acquire videos of the MCP movement, and a screen to display the visual interface to the subject. A digital port on the exoskeleton electronic board was used to switch on a LED, which was framed by the camera, to synchronize the exoskeleton data with videos for offline processing. Custom colored markers, easily recognizable through video analysis, were placed in predefined positions on the robot kinematic chain and the subjects' index fingers. Markers were used to compute offline, through video analysis, the MCP joint angle, which was used as a 'ground truth' to assess the accuracy of the real-time angle estimation through the DKM, as well as for computing the geometric parameters  $a$ ,  $b$ , and  $c$ . In total, nine markers were placed on the robot and the user. Two markers were placed on the user's finger, along the longitudinal axis of the proximal phalanx ( $F1$ ,  $F2$ ). Six markers were placed on the robot kinematic chain, in correspondence with the four hinges ( $O$ ,  $A$ ,  $B$ ,  $C$ ), the slider-hinge joint ( $P$ ) and on the finger cuff base ( $G$ ). Finally, a so-called 'auxiliary marker' ( $O_{aux}$ ) was placed on the user's finger MCP joint, identified through palpation.

### B. Offline Video Analysis

Recorded videos from the digital camera were post-processed in Python environment (v3.9.1) using OpenCV libraries to extract the markers' trajectories during finger motion. The two markers  $F1$  and  $F2$  were used to identify offline the ICR of the user's joint (red dot in Fig. 6), and therefore, compute the finger's MCP angle ( $\theta_{video}^{MCP}$ ) used as the 'ground truth' for the assessment of the robot's accuracy in estimating the joint angle. In particular, the position of the ICR was found via a least-square algorithm that iteratively scanned video frames during F/E movements, and, at each iteration, updated the position of the ICR as the point that minimized the distance with the set of straight lines identified by the two phalanx markers. The ICR position was initialized to the position of the marker  $O_{aux}$  and then updated. Also, for each frame, the parameter  $a_{video}$  was computed as the distance between the marker  $G$  and the estimated ICR, parameter  $b_{video}$  was computed as the distance between marker  $P$  and marker  $G$  and parameter  $c_{video}$  as the distance between the marker  $O$  and the estimated ICR. A synchronization signal (*synch*) was used to allow an offline comparison of data coming from the video and the exoskeleton. This *synch* was based on a Boolean signal implemented in hardware using a LED, which was turned on when the trial started. This signal was saved in a binary file on the exoskeleton board and used offline to cut the video frames before further analyses were conducted. Markers and  $\theta_{video}^{MCP}$ ,  $a_{video}$ ,  $b_{video}$ , and  $c_{video}$  trajectories were saved into a separate file for further analysis and comparison with the robot data.

### C. Experimental Protocol

Both experimental sessions started with a calibration procedure, necessary to generate the user-specific LUT, followed by a testing phase.

1) *Calibration Procedure*: The participant was first asked to wear the exoskeleton with the support of an experimenter, who selected the most appropriate hand and finger cuffs based on the hand's anthropometry. Then, the user was requested to perform about ten repetitions of finger F/E movements with the exoskeleton turned off. Video recordings were downloaded and processed offline. The convergence criterion for the calibration phase was set as when the variation of the ICR position was lower than 0.05 mm for at least three consecutive movements; when the convergence criterion was met, the video analysis was stopped and  $a_{est}$ ,  $b_{est}$ , and  $c_{est}$  were computed as the averages of the  $a_{video}$ ,  $b_{video}$ , and  $c_{video}$  trajectories over at least three movements (Fig. 6). Using the three parameters, the corresponding LUTs for the DKM and IKsM were generated and uploaded to the robot firmware for online use. The calibration phase lasted about 5 minutes.

2) *Testing Phase: First Session*: For the first testing session, subjects were asked to perform a sequence of twenty repetitions of finger F/E movements in *zero-torque* modality within a fixed ROM of 70 deg, following a minimum-jerk reference profile (peak velocity 10 deg/s) displayed on the visual interface. Data from the exoskeleton sensors and the digital camera was collected.

3) *Testing Phase: Second Session*: In the second session, for the torque-tracking experiments, the participants were asked not to contribute actively to the movement while a desired MCP torque profile ( $\tau_{des}^{MCP}$ ) was commanded. The  $\tau_{des}^{MCP}$  signal consisted of twenty sine waves of amplitude 0.05 Nm ( $\tau_{desAmp1}^{MCP}$ ) and 0.1 Nm ( $\tau_{desAmp2}^{MCP}$ ), frequency of 0.25 Hz and an offset of 0.15 Nm. The frequency was selected to mimic a quasi-static motion of the finger.

To evaluate the *transparency* of the system, the subjects were then asked to perform F/E cycles in *zero-torque* modality following a chirp reference signal displayed on the screen, spanning from 0.1 to 1 Hz with an amplitude of 70 deg. The digital camera was not used in this testing session.

#### D. Data Analysis

Data were analyzed using MATLAB (MATLAB 2021a, The MathWorks, Inc., Natick, MA, United States). For the first session, data acquired by the exoskeleton platform and camera were aligned using the *synch* digital signal and then segmented into F/E cycles using the sigmoidal reference profile displayed by the visual interface. The cycles in which marker trajectories were discontinuous due to full or partial coverage of the markers in the video recordings were discarded from the analysis. For each F/E cycle, the 'ground truth',  $\theta_{video}^{MCP}$  computed from the video analysis, and the angle estimated online by the robot,  $\theta_{est}^{MCP}$ , were fitted into a linear model. The coefficient of determination ( $r^2$ ) was calculated to assess the goodness of fit. The  $RMSE_\theta$  between the fitted line and the identity line was computed as a measurement of the accuracy of the robot estimation. In addition, the two variables were used to perform the Bald-Altman regression analysis and compute the Bias and limits of agreements (LoA).

For each subject,  $a_{video}$ ,  $b_{video}$ , and  $c_{video}$  trajectories were computed on F/E movements and the scatter data

( $a_{video}$ ,  $\theta_{video}^{MCP}$ ), ( $b_{video}$ ,  $\theta_{video}^{MCP}$ ), and ( $c_{video}$ ,  $\theta_{video}^{MCP}$ ) were used to compute average profiles, which in turn were used to calculate the  $RMSE$  against the values  $a_{est}$ ,  $b_{est}$ , and  $c_{est}$  computed during the calibration phase and used online by the robot. The  $RMSE$  of the parameters were used to explain the accuracy of the angle estimation. Markers' trajectories were used to compute the angle between segments  $PG$  and  $GO$  (parameter  $\angle(a, b)$ ), to verify that the hypothesis of perpendicularity between the two segments was maintained during the use.

For the second session, the torque tracking performance was assessed by calculating the  $RMSE_\tau$  between  $\tau_{desAmp1,2}^{MCP}$  and  $\tau_{est}^{MCP}$ , computed as in (12). Moreover, the *transparency* of the system in *zero-torque* modality was assessed in terms of residual torques by computing the  $RMSE_\tau$  between  $\tau_{est}^{MCP}$  profile and the null desired signal ( $\tau_{des0}^{MCP}$ ). *Transparency* was also assessed in terms of output impedance (i.e., residual stiffness) in the frequency domain, by computing the descriptive transfer function  $W(s) = \tau_{est}^{MCP} / \theta_{est}^{MCP}$ .

Between-subjects analysis was performed to quantify the overall variation of the  $RMSE_\theta$ ,  $RMSE$  of the geometric parameters,  $\angle(a, b)$  mean values and  $RMSE_\tau$ . The results are reported as median values and interquartile ranges.

#### E. Results

Fig. 7 shows the results of the angle accuracy assessment and Bald-Altman regression analysis for one representative subject. The analysis was performed for every recruited subject. Considering the best-performing subject in the pool, the linear regression model for  $\theta_{est}^{MCP}$  had  $r^2 = 0.999$ , and the Balt-Altman analysis resulted in a Bias of 0.04 deg and an LoA of 2.89 deg; for the worst-performing one, the  $r^2$  of the linear regression for  $\theta_{est}^{MCP}$  was 0.997, and the Balt-Altman analysis resulted in a Bias of -4.37 deg and an LoA of 3.05 deg.

Fig. 8 shows the results of the parameters accuracy analysis for one representative subject. For this subject, scatter plots of  $a_{video}$ ,  $b_{video}$ ,  $c_{video}$  and  $\angle(a, b)$  resulted in relatively high variability of  $a_{video}$  and  $\angle(a, b)$  parameters over the range of movement, whereas  $b_{video}$  and  $c_{video}$  resulted less variable.

Fig. 9 shows the results of torque tracking for one representative subject, together with the estimation of the residual stiffness at the joint level.  $RMSE_\tau$  for this subject was 4.7 mNm for the  $\tau_{desAmp1}^{MCP}$ , and 7.4 mNm for the  $\tau_{desAmp2}^{MCP}$ . The amplitude of the Bode plot shows a magnitude of -52.2 dB at 0.1 Hz and up to -34.3 dB at 1 Hz for the residual output impedance.

Fig. 10 shows the  $RMSE$  and error parameters aggregated between all participants. Overall, the  $RMSE_\theta$  ranged between 0.97 and 4.45 deg, with a median of 1.33 deg. The  $RMSE$  of the geometrical parameters,  $a_{est}$ ,  $b_{est}$ , and  $c_{est}$ , was lower than 3 mm across subjects (medians were 1.71 mm, 0.33 mm, and 2.23 mm, respectively). The range of  $\angle(a, b)$  parameter spanned between 82.32 deg and 90.49 deg, with a median value between subjects of 87.89 deg. In *zero-torque* mode ( $\tau_{des0}^{MCP}$ ), the  $RMSE_\tau$  ranged between 5.49 mNm and 6.2 mNm, with a median value of 5.76 mNm across subjects. Regarding torque tracking performance, for  $\tau_{desAmp1}^{MCP}$



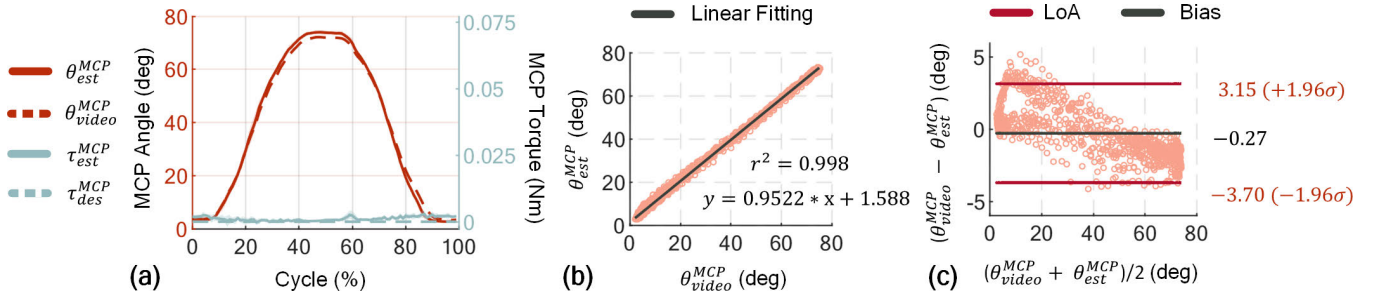


Fig. 7. Results of one representative subject. (a) The mean profiles of the estimated angle from the exoskeleton ( $\theta_{est}^{MCP}$ ) and angle from the video ground truth ( $\theta_{video}^{MCP}$ ) are compared, together with the desired null torque profile ( $\tau_{des}^{MCP}$ ) and the estimated torque at MCP joint ( $\tau_{est}^{MCP}$ ) over the F/E cycle. (b) Linear fitting plots on the angle profiles, where line equations and coefficient of determination ( $r^2$ ) are reported. (c) Bland-Altman plots, showing the Limits of Agreement (LoA) and the Bias of the data.

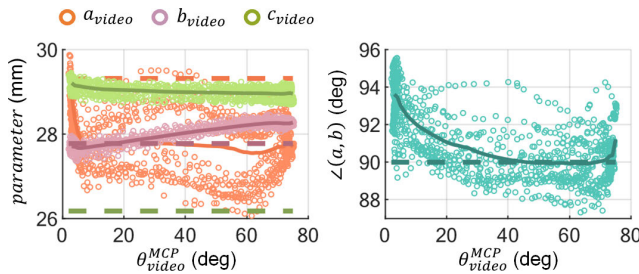


Fig. 8. Analysis of the average parameter profiles for one representative subject.  $a_{video}$ ,  $b_{video}$ ,  $c_{video}$  are the video collected values of the geometric parameters over the entire trial, while  $\theta_{video}^{MCP}$  represents the video ground truth of the MCP angle. Solid lines represent the average value of the parameter, while dashed lines represent the calibration values  $a_{est}$ ,  $b_{est}$  and  $c_{est}$  extracted during the calibration phase.

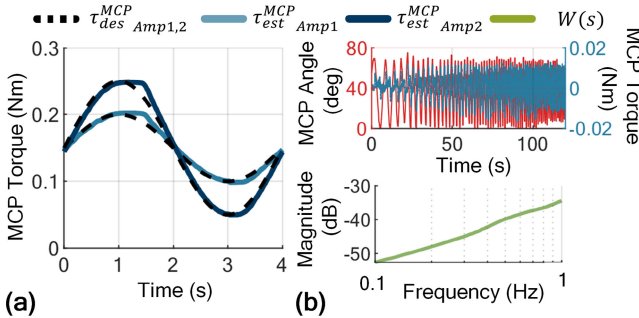


Fig. 9. Analysis of the estimated MCP torque for one representative subject. (a) Mean profiles estimated over twenty cycles. (b) Estimated residual stiffness at the joint level during zero-torque modality and the magnitude of the residual stiffness transfer function  $W(s)$ .

the  $RMSE_{\tau}$  ranged between 4.7 mNm and 4 mNm, with a median value of 4.4 mNm across subjects, while for  $\tau_{des}^{MCP}$  the  $RMSE_{\tau}$  ranged between 7.4 mNm and 6.2 mNm, with a median value of 6.85 mNm across subjects.

## VI. DISCUSSION

In robotic devices for post-traumatic hand rehabilitation, kinematic compatibility is key for effective and safe torque transfer to the human joints, the axes of which are both difficult to identify and not-fixed during movements due to joint laxity [25]. Range of motion, encumbrance, and adaptability of the device to different hand anthropometries are also important aspects to consider in the design. Concerning functionalities, hand rehabilitation robots should be able to perform repetitive mobilization of the joints, to treat the joint stiffness that

often characterizes post-traumatic and post-operative conditions (e.g., due to impaired tendon gliding or capsule fibrosis). Among all hand joints, the rigidity of the MCP (typically in an extended position) is the most disabling condition, as the MCP range of motion accounts for most of the movement in pinching and grasping tasks in daily activities. Hence, the majority of the effort, usually, is spent on the mobilization of this joint [26]. In this work, a novel self-aligning kinematic chain for the F/E mobilization of a human joint has been presented, together with its implementation on a finger exoskeletal platform for MCP rehabilitation. The chain has an RPR architecture, characterized by the decomposition of the first rotational joint into a series of hinges, to accommodate for a physiological ROM of the finger within a compact structure. The RRP structure, with the prismatic joint housed on the finger, is employed by similar systems in recent literature [27], [28]. Here, an RPR architecture was preferred because it provides for a slider with a stroke independent of the first phalanx's length and can thus accommodate various anthropometries. In terms of encumbrance, the wearable parts of the platform, including the kinematic chain and the proximal cuff on the phalanx, are included in a volume of 28.66 cm<sup>3</sup> (88.26 × 26.75 × 12.14 mm), resulting in a compact design similar to the literature [29], [30] and in line with the acceptable encumbrance of 75 cm<sup>3</sup> (50 × 50 × 30 mm) for the whole hand proposed in [31].

Considering the performance of the torque control, bench tests showed a closed-loop torque bandwidth higher than 5 Hz. In other studies, similar devices resulted to be suitable for a clinical application even with a lower bandwidth [7], [16], thus suggesting the applicability of the presented actuation system in the ecological scenario. Output mechanical impedance at the SEA unit resulted equal to 0.17 Nm/rad at 1 Hz, which is 15 times lower than the nominal spring stiffness used in the SEA.

Human-in-the-loop experiments were performed to verify the kinematic model and to quantify the estimated torque at the MCP joint both in *zero-torque* modality and in torque tracking experiments. The estimated joint angle showed a  $RMSE$  of 1.33 deg between subjects, lower than 2% of the full range of motion. The torque  $RMSE$ , always below 7 mNm in *zero-torque* modality and below 8 mNm in torque-tracking experiments, can be considered negligible in clinical applications in which the patient has to move actively [4], [32],

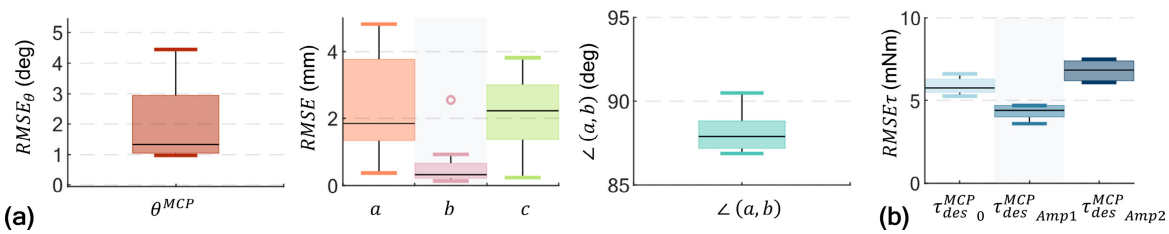


Fig. 10. (a). Between-subjects analysis of  $RMSE_{\theta}$ ,  $RMSE$  of the geometric parameters  $a$ ,  $b$  and  $c$  with respect to the calibration values, and variation of orthogonality condition between the segments  $a$  and  $b$  ( $\angle(a, b)$ ). (b) MCP torque  $RMSE_{\tau}$  in zero-torque modality ( $\tau_{des_0}^{MCP}$ ) and for the two sinusoidal desired MCP profiles  $\tau_{des_{Amp1}}^{MCP}$  (0.05 Nm amplitude) and  $\tau_{des_{Amp2}}^{MCP}$  (0.1 Nm amplitude) with a frequency of 0.25 Hz.

and demonstrate a proper torque transfer at the joint level for the intended operation of the device. The performance of the angle and torque estimation at the joint level is comparable to those reported in previous studies [33], [34] and suggests that the exoskeleton can provide reliable measurements of biomechanical parameters relevant to the safe treatment and evaluation of the MCP joint. A limitation of the current approach for MCP torque estimation is that it is grounded on the VWP method, which holds under quasi-static conditions. This assumption may not be adequate in some rehabilitation scenarios. To overcome this limitation, other strategies (e.g., Jacobian computation, and inverse dynamic models) can be considered.

The geometric parameters that were computed through video analyses on the testing trials ( $a_{video}$ ,  $b_{video}$ ,  $c_{video}$ ) resulted in slightly different than the values computed during the calibration phase ( $a_{est}$ ,  $b_{est}$ , and  $c_{est}$ ), with differences up to 5 mm for parameter  $a$ . These differences could be explained by two main factors: first, the interfaces can move slightly during the operation of the device, therefore the geometric parameters can change during use; second, the ‘ground truth’, namely the parameters computed from the video analysis using the markers can suffer from the movement of the markers on the soft tissues of the articulations. Notably, parameter  $\angle(a, b)$  showed values in the range between 85 and 90 deg for all subjects, confirming that the chain of passive degrees of freedom ensures a correct alignment to the phalanx, and friction effects are overall negligible on the chain. Overall, the limited variability of the error values of the four geometric parameters suggests that the model holds under the operation of the device.

Future developments will focus on improving the actuation performance to provide higher and bidirectional (flexor and extensor) torque at the MCP joint and on the applicability of the mechanism to multiple fingers. Also, the possibility to move the hand in the space will be considered, to enable the execution of functional tasks, such as those of activities of daily living.

## REFERENCES

- [1] L. Ye, L. Kalichman, A. Spittle, F. Dobson, and K. Bennell, “Effects of rehabilitative interventions on pain, function and physical impairments in people with hand osteoarthritis: A systematic review,” *Arthritis Res. Therapy*, vol. 13, no. 1, pp. 1–13, Feb. 2011, doi: 10.1186/ar3254.
- [2] G. Yang, E. P. McGlenn, and K. C. Chung, “Management of the stiff finger,” *Clinics Plastic Surg.*, vol. 41, no. 3, pp. 501–512, Jul. 2014, doi: 10.1016/j.cps.2014.03.011.
- [3] S. L. Moran and R. A. Berger, “Biomechanics and hand trauma: What you need,” *Hand Clinics*, vol. 19, no. 1, pp. 17–31, 2003, doi: 10.1016/S0749-0712(02)00130-0.
- [4] D. Marconi, A. Baldoni, Z. McKinney, M. Cempini, S. Crea, and N. Vitiello, “A novel hand exoskeleton with series elastic actuation for modulated torque transfer,” *Mechatronics*, vol. 61, pp. 69–82, Aug. 2019, doi: 10.1016/j.mechatronics.2019.06.001.
- [5] P. Heo, G. M. Gu, S. Lee, K. Rhee, and J. Kim, “Current hand exoskeleton technologies for rehabilitation and assistive engineering,” *Int. J. Precis. Eng. Manuf.*, vol. 13, no. 5, pp. 807–824, 2012, doi: 10.1007/s12541-012-0107-2.
- [6] D. Popov, I. Gaponov, and J. H. Ryu, “Portable exoskeleton glove with soft structure for hand assistance in activities of daily living,” *IEEE/ASME Trans. Mechatron.*, vol. 22, no. 2, pp. 865–875, Apr. 2017, doi: 10.1109/TMECH.2016.2641932.
- [7] M. Xiloyannis, L. Cappello, D. Binh Khanh, S.-C. Yen, and L. Masia, “Modelling and design of a synergy-based actuator for a tendon-driven soft robotic glove,” in *Proc. 6th IEEE Int. Conf. Biomed. Robot. Biomechatronics (BioRob)*, Singapore, Jun. 2016, pp. 1213–1219, doi: 10.1109/BIOROB.2016.7523796.
- [8] T. Bützer, O. Lamberg, J. Arata, and R. Gassert, “Fully wearable actuated soft exoskeleton for grasping assistance in everyday activities,” *Soft Robot.*, vol. 8, no. 2, pp. 128–143, Apr. 2021, doi: 10.1089/soro.2019.0135.
- [9] L. Cappello et al., “Exploiting textile mechanical anisotropy for fabric-based pneumatic actuators,” *Soft Robot.*, vol. 5, no. 5, pp. 662–674, 2018, doi: 10.1089/soro.2017.0076.
- [10] C. Qin, P. Li, X. Yang, and B. Li, “A design of hand rehabilitation exoskeleton mechanism adapted to different finger lengths,” in *Proc. IEEE Int. Conf. Robot. Biomimetics (ROBIO)*, Dec. 2019, pp. 1621–1626, doi: 10.1109/ROBIO49542.2019.8961694.
- [11] E. Capotorti et al., “A novel torque-controlled hand exoskeleton to decode hand movements combining Semg and fingers kinematics: A feasibility study,” *IEEE Robot. Autom. Lett.*, vol. 7, no. 1, pp. 239–246, Jan. 2022, doi: 10.1109/LRA.2021.3111412.
- [12] M. Cempini, S. M. M. de Rossi, T. Lenzi, N. Vitiello, and M. C. Carrozza, “Self-alignment mechanisms for assistive wearable robots: A kinetostatic compatibility method,” *IEEE Trans. Robot.*, vol. 29, no. 1, pp. 236–250, Feb. 2013, doi: 10.1109/TRO.2012.2226381.
- [13] M. B. Näf, K. Junius, M. Rossini, C. Rodriguez-Guerrero, B. Vanderborght, and D. Lefeber, “Misalignment compensation for full human-exoskeleton kinematic compatibility: State of the art and evaluation,” *Appl. Mech. Rev.*, vol. 70, no. 5, pp. 1–19, Sep. 2018, doi: 10.1115/1.4042523.
- [14] M. Sarac, M. Solazzi, and A. Frisoli, “Design requirements of generic hand exoskeletons and survey of hand exoskeletons for rehabilitation, assistive, or haptic use,” *IEEE Trans. Haptics*, vol. 12, no. 4, pp. 400–413, Oct. 2019, doi: 10.1109/TOH.2019.2924881.
- [15] M. Cempini et al., “Kinematics and design of a portable and wearable exoskeleton for hand rehabilitation,” in *Proc. IEEE 13th Int. Conf. Rehabil. Robot. (ICORR)*, Seattle, WA, USA, Jun. 2013, pp. 1–6, doi: 10.1109/ICORR.2013.6650414.
- [16] P. Agarwal, J. Fox, M. K. O’Malley, A. D. Deshpande, and Y. Yun, “An index finger exoskeleton with series elastic actuation for rehabilitation: Design, control and performance characterization,” *Int. J. Robot. Res.*, vol. 34, no. 14, pp. 1747–1772, Oct. 2015, doi: 10.1177/0278364915598388.

- [17] F. C. T. H. H. A. van der Arno Stienen, E. G. Eds.,ko Hekman, and H. van der Kooij, "Self-aligning exoskeleton axes through decoupling of joint rotations and translations," *IEEE Trans. Robot.*, vol. 25, no. 3, pp. 628–633, Jun. 2009, doi: [10.1109/TRO.2009.2019147](https://doi.org/10.1109/TRO.2009.2019147).
- [18] W. J. Barnes and J. D. Allison, "Isometric torque of the finger extensors at the metacarpophalangeal joints," *Phys. Therapy*, vol. 58, no. 1, pp. 42–45, Jan. 1978, doi: [10.1093/ptj/58.1.42](https://doi.org/10.1093/ptj/58.1.42).
- [19] M. Vergara, M. J. Agost, and V. Gracia-Ibáñez, "Dorsal and palmar aspect dimensions of hand anthropometry for designing hand tools and protections," *Hum. Factors Ergonom. Manuf. Service Industries*, vol. 28, no. 1, pp. 17–28, Jan. 2018, doi: [10.1002/hfm.20714](https://doi.org/10.1002/hfm.20714).
- [20] N. Vitiello, A. Baldoni, S. Crea, A. Scalamogna, and T. Fiumalbi, *Kinematic Chain to Assist Flexion-Extension of a Joint*, document IT102019000017558, Sep. 2019.
- [21] M. C. Carrozza, N. Vitiello, M. Cempini, and F. Giovacchini, *Torsional Transmission Element With Elastic Response*, document ITFI2013A000156, Jul. 2013.
- [22] H. Hayashi and H. Shimizu, "Essential motion of metacarpophalangeal joints during activities of daily living," *J. Hand Therapy*, vol. 26, no. 1, pp. 69–74, Jan. 2013, doi: [10.1016/j.jht.2012.10.004](https://doi.org/10.1016/j.jht.2012.10.004).
- [23] J. A. Haarman, J. Reenalda, J. H. Buurke, H. van der Kooij, and J. S. Rietman, "The effect of 'device-in-charge' versus 'patient-in-charge' support during robotic gait training on walking ability and balance in chronic stroke survivors: A systematic review," *J. Rehabil. Assistive Technol. Eng.*, vol. 3, Jan. 2016, Art. no. 205566831667678, doi: [10.1177/2055668316676785](https://doi.org/10.1177/2055668316676785).
- [24] J. Pan et al., "NESM- $\gamma$ : An upper-limb exoskeleton with compliant actuators for clinical deployment," *IEEE Robot. Autom. Lett.*, vol. 7, no. 3, pp. 7708–7715, Jul. 2022, doi: [10.1109/LRA.2022.3183926](https://doi.org/10.1109/LRA.2022.3183926).
- [25] I. M. Bullock, J. Borrás, and A. M. Dollar, "Assessing assumptions in kinematic hand models: A review," in *Proc. 4th IEEE RAS EMBS Int. Conf. Biomed. Robot. Biomechatronics (BioRob)*, Jun. 2012, pp. 139–146, doi: [10.1109/BioRob.2012.6290879](https://doi.org/10.1109/BioRob.2012.6290879).
- [26] M. A. Hardy, "Principles of metacarpal and phalangeal fracture management: A review of rehabilitation concepts," *J. Orthopaedic Sports Phys. Therapy*, vol. 34, no. 12, p. 19, Dec. 2004, doi: [10.2519/jospt.2004.1524](https://doi.org/10.2519/jospt.2004.1524).
- [27] N. Sun, G. Li, and L. Cheng, "Design and validation of a self-aligning index finger exoskeleton for post-stroke rehabilitation," *IEEE Trans. Neural Syst. Rehabil. Eng.*, vol. 29, pp. 1513–1523, 2021, doi: [10.1109/TNSRE.2021.3097888](https://doi.org/10.1109/TNSRE.2021.3097888).
- [28] G. Li, L. Cheng, Z. Gao, X. Xia, and J. Jiang, "Development of an untethered adaptive thumb exoskeleton for delicate rehabilitation assistance," *IEEE Trans. Robot.*, vol. 38, no. 6, pp. 3514–3529, Dec. 2022, doi: [10.1109/TRO.2022.3180832](https://doi.org/10.1109/TRO.2022.3180832).
- [29] D. Wang, Q. Meng, Q. Meng, X. Li, and H. Yu, "Design and development of a portable exoskeleton for hand rehabilitation," *IEEE Trans. Neural Syst. Rehabil. Eng.*, vol. 26, no. 12, pp. 2376–2386, Dec. 2018, doi: [10.1109/TNSRE.2018.2878778](https://doi.org/10.1109/TNSRE.2018.2878778).
- [30] P. Esmatloo and A. D. Deshpande, "Fingertip position and force control for dexterous manipulation through model-based control of hand-exoskeleton-environment," in *Proc. IEEE/ASME Int. Conf. Adv. Intell. Mechatronics (AIM)*, Boston, MA, USA, Jul. 2020, pp. 994–1001, doi: [10.1109/AIM43001.2020.9158879](https://doi.org/10.1109/AIM43001.2020.9158879).
- [31] Q. A. Boser, M. R. Dawson, J. S. Schofield, G. Y. Dziwenko, and J. S. Hebert, "Defining the design requirements for an assistive powered hand exoskeleton: A pilot explorative interview study and case series," *Prosthetics Orthotics Int.*, vol. 45, no. 2, pp. 161–169, Apr. 2021, doi: [10.1177/0309364620963943](https://doi.org/10.1177/0309364620963943).
- [32] J. F. Veneman, R. Ekkelenkamp, R. Kruidhof, F. C. T. Van Der Helm, and F. C. T. Van Der Helm, "A series elastic- and Bowden-cable-based actuation system for use as torque actuator in exoskeleton-type robots," *Int. J. Robot. Res.*, vol. 25, no. 3, pp. 261–281, Mar. 2006, doi: [10.1177/0278364906063829](https://doi.org/10.1177/0278364906063829).
- [33] A. Di Guardo, M. Sarac, M. Gabardi, D. Leonardi, M. Solazzi, and A. Frisoli, "Sensitivity analysis and identification of human parameters for an adaptive, underactuated hand exoskeleton," in *Advances in Robot Kinematics 2018*, vol. 8, J. Lenarcic and V. Parenti-Castelli, Eds. Cham, Switzerland: Springer, 2018, pp. 449–457, doi: [10.1007/978-3-319-93188-3\\_51](https://doi.org/10.1007/978-3-319-93188-3_51).
- [34] R. Casas, K. Martin, M. Sandison, and P. S. Lum, "A tracking device for a wearable high-DOF passive hand exoskeleton," in *Proc. 43rd Annu. Int. Conf. IEEE Eng. Med. Biol. Soc. (EMBC)*, Mexico, Nov. 2021, pp. 6643–6646, doi: [10.1109/EMBC46164.2021.9630403](https://doi.org/10.1109/EMBC46164.2021.9630403).

Open Access funding provided by 'Scuola Superiore "S. Anna" di Studi Universitari e di Perfezionamento' within the CRUI CARE Agreement